Resolution of zigzag magnetic correlations in Na-deficient Na$_x$IrO$_3$ without long-range ordering

Jungho Kim [1,*] Hengdi Zhao [2] and Gang Cao[2]

[1]*Advanced Photon Source, Argonne National Laboratory, Argonne, Illinois 60439, USA*
[2]*Department of Physics, University of Colorado at Boulder, Boulder, Colorado 80309, USA*

The materials search for Kitaev quantum spin liquids led to the discovery of many honeycomb lattice materials. Much attention has been paid to materials without magnetic order down to the lowest temperatures. The newly synthesized Na-deficient Na$_x$IrO$_3$ has been found to bear no sign of long-range magnetic order above 1 K from physical property measurements. In this paper, we report momentum- and energy-resolved excitation spectra in Na-deficient Na$_x$IrO$_3$ measured using a resonant inelastic x-ray scattering spectrometer. Orbital excitation spectra show that the octahedral and trigonal crystal field splittings are larger in Na$_x$IrO$_3$ than in Na$_2$IrO$_3$. On the other hand, the low-energy spectrum at low temperature shows a wave-vector dispersion and a spectral weight distribution that are similar to those of Na$_2$IrO$_3$, revealing that the two-dimensional zigzag magnetic correlations in Na$_x$IrO$_3$ are similar to those in Na$_2$IrO$_3$ in terms of the ordered magnetic moment direction and three dynamically fluctuating zigzag orders. The azimuth angle dependence of the low-energy spectrum corroborates these results. The two-dimensional zigzag magnetic correlations rapidly weaken until 50 K. At high temperatures, the spectral weight distribution of the low-energy excitation resembles that of the pure Kitaev model, indicating that the Kitaev interaction dominates the dynamic magnetic response at high temperature. We suggest that the larger crystal field and distortion and the weakened longer-range Heisenberg exchange interactions due to the Na deficiency in Na$_x$IrO$_3$ contribute to bring Na$_x$IrO$_3$ away from the zigzag long-range magnetic order phase.

I. INTRODUCTION

A_2IrO$_3$-type (A = alkali) layered materials where half-integer-spin Ir ions form a honeycomb lattice have received much attention since Jackeli and Khaliullin proposed the Kitaev model with a quantum-spin-liquid ground state [1]. Na$_2$IrO$_3$ is one of the first and most extensively studied candidate materials for the Kitaev quantum spin liquid (KQSL) [2–5]. The KQSL is not realized, but a conventional symmetry-breaking zigzag magnetic order is found in Na$_2$IrO$_3$. The spin model includes nearest-neighbor Heisenberg and symmetric off-diagonal exchange interactions and long-range exchange interactions to explain the observed zigzag order [6–9]. Nonetheless, the Kitaev-Heisenberg (KH) model and related spin models indicate an extended spin-liquid phase near the pure Kitaev limit [6,7,10–13], which widens the scope of candidate materials.

A Na-deficient Na$_x$IrO$_3$ ($0.6 \leqslant x \leqslant 0.8$) single crystal has been synthesized [14]. The structure refinement found that Na$_x$IrO$_3$ adopts a layered honeycomb lattice without stacking disorder and all Na vacancies occur at the site of the center position of the honeycomb ring. Na$_x$IrO$_3$ has an equal Ir-Ir bond length between neighboring Ir ions which is larger than two unequal Ir-Ir bond lengths of Na$_2$IrO$_3$. The Ir-O bond length in Na$_x$IrO$_3$ is shorter than that in Na$_2$IrO$_3$. The compression along the c axis of Na$_x$IrO$_3$ is larger than that of

Na$_2$IrO$_3$, indicating a larger trigonal distortion. Interestingly, the physical property measurements found no sign of a long-range magnetic order above 1 K in Na$_x$IrO$_3$, which possibly points to an exotic ground state in proximity to a possible KQSL.

Resonant inelastic x-ray scattering (RIXS) measurements have provided important information on orbital and magnetic structures of Na$_2$IrO$_3$ [15–18]. Diffuse magnetic scattering data obtained by the RIXS technique revealed dynamically fluctuating zigzag orders which are directly connected to the Kitaev physics [17]. Direct comparison of high-resolution RIXS spectra and theoretical simulations could confine a parameter regime of the extended Kitaev-Heisenberg model for Na$_2$IrO$_3$ [18]. Here, we study the Na-deficient Na$_x$IrO$_3$ to reveal orbital and magnetic states of Na$_x$IrO$_3$ using RIXS measurements. Orbital excitation spectra show that the octahedral and trigonal crystal field splittings are larger in Na$_x$IrO$_3$ than in Na$_2$IrO$_3$, which is expected considering that Na$_x$IrO$_3$ has a shorter Ir-O bond length and larger trigonal distortion than Na$_2$IrO$_3$. The main finding from the low-energy spectrum at low temperature is that the magnetic ground state of Na$_x$IrO$_3$ is described by two-dimensional zigzag magnetic correlations that are similar to those of Na$_2$IrO$_3$. At high temperatures, the two-dimensional zigzag magnetic correlation is largely weakened, and the spectral weight distribution of the low-energy excitation resembles that of the pure Kitaev model, indicating that the Kitaev interaction dominates the dynamic magnetic response at high temperature.

*jhkim@aps.anl.gov

075157-1

II. SAMPLE AND RIXS MEASUREMENT

Single crystals of Na_xIrO_3 were grown by the self-flux method [14]. The sample was mounted in a Displex closed-cycle cryostat. The RIXS measurements were performed using the RIXS spectrometer at the 27-ID beamline of the Advanced Photon Source, where the sample, analyzer, and detector are positioned in the Rowland geometry. The diamond(111) high-heat-load monochromator reflects x rays from two in-line undulators into a high-resolution monochromator. The two-bounce monochromator of single monolithic Si(844) channel-cut crystal produces an energy bandpass of 14.8 meV. The beam is then focused by a set of Kirkpatrick-Baez mirrors, yielding a typical spot size of 10×40 μm^2 full width at half maximum (FWHM; vertical × horizontal) at the sample. A horizontal scattering geometry was used with the incident photon polarization in the scattering plane. Mapping of the full Brillouin zone was carried out within only a few degrees of the 90° scattering geometry to minimize the contribution from the Thomson elastic scattering. For the 25-meV RIXS measurement, a Si(844) diced spherical analyzer with 2-in. diameter and a position-sensitive silicon microstrip detector were used.

III. RESULTS

A. Wide-energy-range RIXS spectra

Figure 1(a) shows an intensity color plot of RIXS spectra at the Brillouin zone center of Na_xIrO_3 across the Ir L_3-edge absorption. The vertical and horizontal axes are the incident photon energy E_i and the energy loss, respectively, in units of eV. The large intensity at zero energy loss is the elastic scattering. Three groups of inelastic resonant features are observed. The feature near the elastic scattering is assigned as magnetic excitations [18,19]. The feature around 1 eV energy loss denoted by "A" is assigned as the orbital excitations within t_{2g} orbitals. These two features resonated at around $E_i = 11\,215$ eV. The high-energy feature around 3.5 eV denoted by "B" is the orbital excitation between t_{2g} and e_g orbitals which resonates at around $E_i = 11\,218$ eV.

Figure 1(b) shows a schematic of the sample and scattering geometry. Red, black, and purple circles represent Ir, O, and Na ions, respectively. A partially filled purple circle indicates the Na deficiency. The crystal structure of Na_xIrO_3 is refined as a two-dimensional hexagonal structure with space group P-$31m$ (No. 162). **a** and **b** denote the lattice vectors. Green arrows indicate the cubic axes (x, y, z) with respect to the octahedra (all of them point above the plane of the paper). Yellow arrows indicate the incident (k_i) and outgoing (k_f) x-ray propagation directions which define the horizontal scattering plane (gray). Brown arrows indicate x-ray polarizations. The azimuth ψ is defined as the angle between the **a** axis and the scattering plane. In this diagram, ψ is 180°. Figure 1(c) shows a two-dimensional reciprocal space diagram. **a*** and **b*** denote the reciprocal lattice vectors. The inner hexagon (blue dashed line) and the outer hexagon (red solid line) indicate the first and second Brillouin zones of the honeycomb lattice, respectively. Magnetic Bragg peak positions of the zigzag orders propagating along three equivalent directions are indicated by M1, M2, and M3. All RIXS measurements were carried
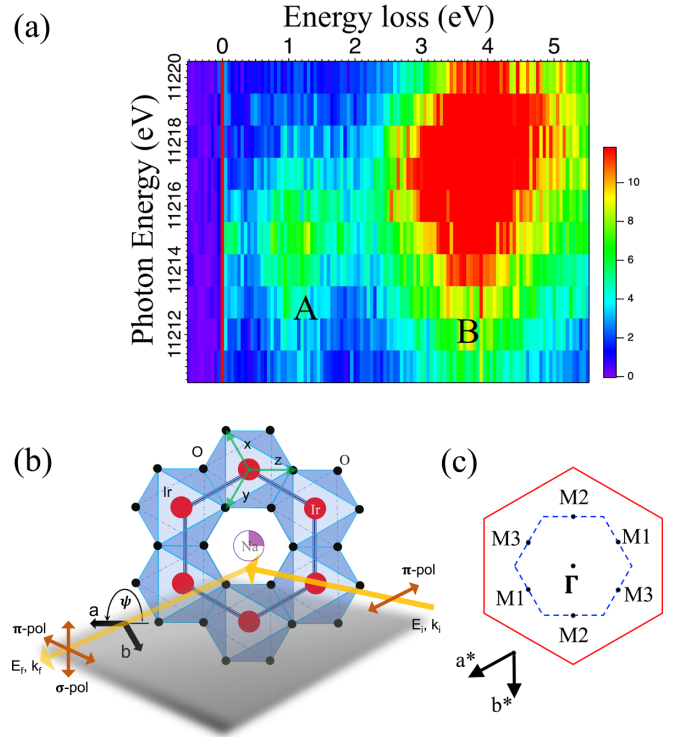

FIG. 1. Incident photon energy dependence and measurement geometry. (a) Intensity color plot of RIXS spectra at the Brillouin zone center of Na_xIrO_3 as functions of the incident photon energy E_i and the energy loss. (b) Schematic of the honeycomb lattice and RIXS scattering geometry. (c) Two-dimensional first (blue dashed line) and second (red solid line) Brillouin zones of the honeycomb lattice.

out with a 90° scattering angle ($k_f \perp k_i$) to minimize elastic scattering. The first Brillouin zone including magnetic Bragg peaks is accessed within 5° of the 45° sample angle.

Figures 2(a) and 2(b) show wide-energy-loss-range RIXS spectra at the Brillouin zone center of Na_xIrO_3 and Na_2IrO_3, respectively, collected with $E_i = 11\,215$ eV. Both spectra consist of the same number of excitation peaks, indicating that Na_xIrO_3 and Na_2IrO_3 share the same electronic structure. The magnetic excitation near the elastic scattering will be discussed in the next section [18,19]. Excitation peaks in region A were fit to three Gaussian functions (red dotted curves) with a broad Gaussian background (blue dashed curves). A broad Gaussian function was used to fit the intermediate energy region. Excitation peaks in region B were fit to three Gaussian functions (red dotted curves) with a broad slope background (blue dashed curves). The resulting peak energies are summarized in Table I.

The sharp peak around 0.5 eV is assigned as a particle-hole excitation across the Mott gap or an intersite excitation arising from the coupling between the particle-hole continuum and the local spin-orbit exciton [15,20]. This peak energy is similar in both materials, indicating that Na_xIrO_3 and Na_2IrO_3 have a similar particle-hole gap. Two peaks around 0.9 eV are attributed to on-site orbital excitations between $J_{eff} = 1/2$ and $3/2$ states [15,20]. The peak energy difference originates from the $J_{eff} = 3/2$ splitting due to the trigonal
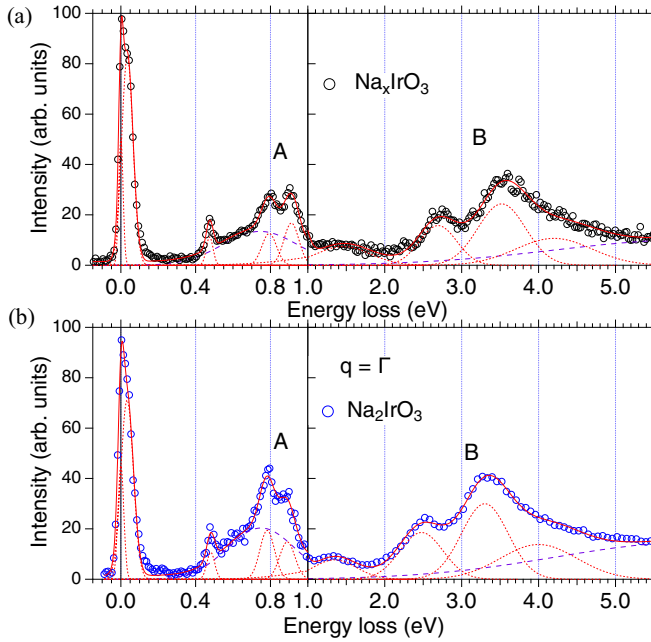
FIG. 2. Wide-range RIXS spectra at the Brillouin zone center. RIXS spectra with $E_i = 11\,215$ eV for Na-deficient Na_xIrO_3 and stoichiometric Na_2IrO_3 are shown in (a) and (b), respectively. Open circles and solid curves indicate the measured RIXS spectra and the result of a fit, respectively. The dotted curves represent Gaussian peaks for a fit. The dashed curves indicate the backgrounds. The resulting peak energies are summarized in Table I.

distortion. As seen in Table I, the energy difference is higher in Na_xIrO_3 (119 meV) than in Na_2IrO_3 (107 meV), indicating that Na_xIrO_3 has a larger trigonal splitting. High energy peaks above 2 eV are associated with on-site orbital excitations between t_{2g} and e_g orbitals, reflecting the octahedral crystal field splitting. These peak energies of Na_xIrO_3 are higher by 0.22 eV than those of Na_2IrO_3, indicating that Na_xIrO_3 has a larger octahedral crystal field splitting. These observations are consistent with the results from the structure refinement that the compression along the c axis of Na_xIrO_3 is larger than that of Na_2IrO_3 and the Ir-O bond length in Na_xIrO_3 is shorter than that in Na_2IrO_3 [14].

B. Low-energy RIXS spectra

1. Two-dimensional zigzag magnetic correlations

Figure 3(a) shows the RIXS intensity image plot of the low-energy magnetic excitation for $\psi = 180°$ as functions of the energy loss and the wave vector. The reciprocal space

TABLE I. Peak energies from a fit in regions A and B shown in Figs. 2(a) and 2(b). All units are eV.

	A			B		
	Peak 1	Peak 2	Peak 3	Peak 1	Peak 2	Peak 3
Na_xIrO_3	0.480	0.793	0.912	2.70	3.52	4.22
Na_2IrO_3	0.475	0.783	0.890	2.48	3.30	4.00

diagram is drawn at the bottom with the measured path along the symmetry directions. The sample and RIXS measurement geometries are the same as those in Ref. [18]. The RIXS intensity map of Na_xIrO_3 shows the same characteristic features: specular elastic scatterings at Γ and Γ', a diffuse quasielastic peak at M1, high low-energy intensity at K, and broad incoherent scattering at Γ. This observation points to the fact that the two-dimensional zigzag magnetic correlations that exist in Na_xIrO_3 are similar to those in Na_2IrO_3 in terms of the ordered magnetic moment direction and three dynamically fluctuating zigzag orders [17]. On the other hand, the L dependence of the quasielastic scattering at M1 shows no peak feature, indicating no long-range magnetic order at 7 K, unlike the case of Na_2IrO_3, as shown in the inset of Fig. 3(b).

Figure 3(b) shows the measured RIXS spectra at all pairs of M1, M2, and M3 positions for $\psi = 180°$. Diffuse quasielastic scattering is absent at M2 but significant at M1 and M3. Figure 3(c) shows schematics of three zigzag orders propagating along three equivalent directions and the corresponding diffuse magnetic scattering pattern for $\psi = 180°$, which were also found in Na_2IrO_3 [17]. The M1, M2, and M3 orders have the zigzag ferromagnetic (FM) chains running along the cubic x, z, and y axes, respectively. The spin moments of each order lie approximately between two other cubic axes perpendicular to each zigzag FM chain axis [17]. For example, the spin moment of the M2 order points roughly in between the cubic x and y axes. At the near-45° sample angle, k_f is approximately halfway between the cubic x and y axes. In the 90° scattering angle geometry, the RIXS spectrometer does not probe spin moments parallel to k_f, but spin moments along k_i and perpendicular to the horizontal scattering plane [17]. So the scattering intensity for the M2 order moment vanishes in the case of $\psi = 180°$ because the spin moments of the M2 order are roughly aligned with k_f. The schematic of the corresponding diffuse magnetic scattering pattern shows large intensities at pairs of M1 and M3 but no intensity at pairs of M2. This pattern is consistent with the measured RIXS spectra in Fig. 3(b).

Figure 3(d) shows the RIXS intensity image plot and reciprocal space diagrams with the measured path along the symmetry directions for $\psi = 210°$. High low-energy intensity at K and a broad incoherent scattering at Γ are similar to the case of $\psi = 180°$. Diffuse quasielastic scattering intensities are observed at both M1 and M3. Figure 3(e) shows that diffuse quasielastic scattering exists at all pairs of M1, M2, and M3 positions with different intensities: strongest at M1, intermediate at M3, and smallest at M2. In the case of $\psi = 210°$, none of the three zigzag orders has spin moment parallel to k_f as shown in Fig. 3(f), and so the three zigzag orders have finite scattering intensities. The observed different intensities at M1, M2, and M3 are consistent with the corresponding diffuse magnetic scattering pattern of three zigzag orders as shown in Fig. 3(f).

The RIXS intensity image plot for $\psi = 300°$ in Fig. 3(g) is identical to that for $\psi = 180°$ in Fig. 3(a). For $\psi = 300°$, diffuse quasielastic scattering is absent at M3 but significant at M1 and M2 as shown in Fig. 3(h). As shown in Fig. 3(i), the spin moments of the M3 order and k_f are both halfway between the cubic z and x axes. So, the scattering intensity
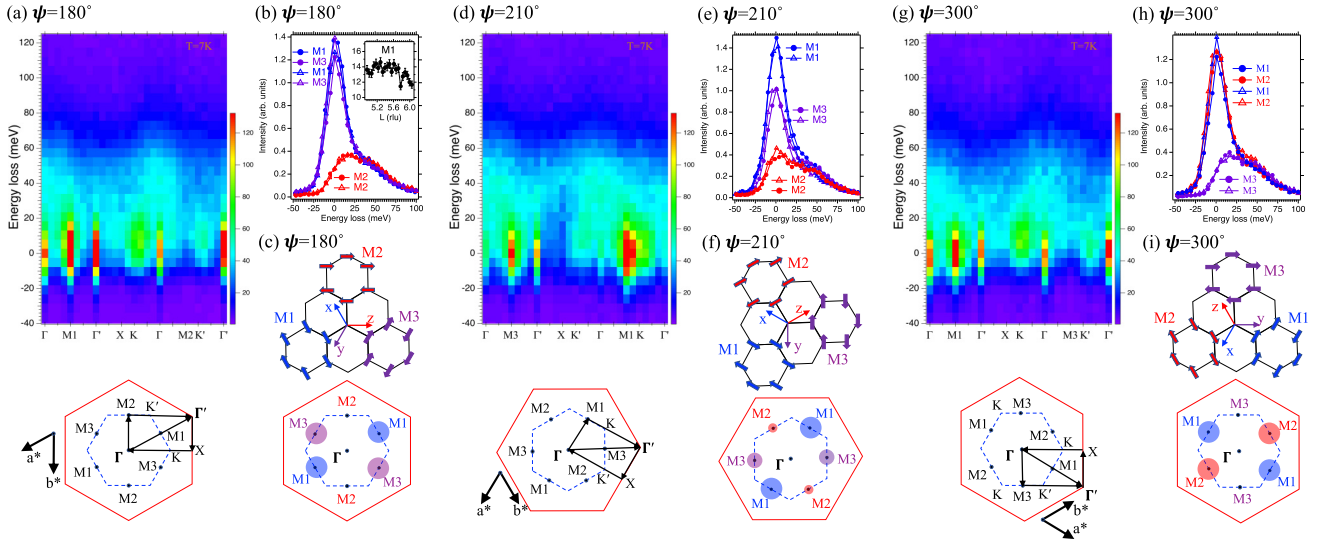
FIG. 3. Magnetic excitation spectra and diffuse magnetic scatterings in Na_xIrO_3 taken at $T = 7$ K. (a), (d), and (g) RIXS intensity maps of magnetic excitations and two-dimensional reciprocal space diagrams with the measured path along the symmetry directions for $\psi = 180°$, $210°$, and $300°$, respectively, as functions of the wave vector and the energy loss. (b), (e), and (h) Measured RIXS spectra at all pairs of M1, M2, and M3 positions for $\psi = 180°$, $210°$, and $300°$, respectively. (c), (f), and (i) Schematics of three zigzag orders propagating along three equivalent directions and corresponding diffuse magnetic scattering patterns for $\psi = 180°$, $210°$, and $300°$, respectively.

for the M3 order moment vanishes. The schematic of the corresponding diffuse magnetic scattering pattern for $\psi = 300°$ is consistent with the observed diffuse quasielastic scattering intensities in Fig. 3(h).

The observation that the three-azimuth-angle low-energy RIXS data for Na_xIrO_3 are consistent with those for Na_2IrO_3 corroborates that Na_xIrO_3 and Na_2IrO_3 share the same two-dimensional (2D) zigzag magnetic order in terms of the ordered magnetic moment direction and three dynamically fluctuating zigzag orders.

2. Temperature evolution of magnetic excitation spectra

Figure 4(a) shows RIXS spectra ($\psi = 180°$) at M1 with increasing temperatures. The diffuse quasielastic scattering peak and the incoherent broad feature were fit to a pseudo-Voigt and a Gaussian function, respectively. The diffuse quasielastic intensity plotted in Fig. 4(c) shows a rapid decrease up to 50 K and a gradual decrease above 50 K. The intensity drop indicates a diminishing 2D zigzag magnetic correlation at high temperature. On the other hand, RIXS spectra ($\psi = 180°$) at M2 consist of only the incoherent broad feature, which shows a marginal change upon temperature increase.

Figures 5(a), 5(b), and 5(c) show RIXS intensity image plots at $T = 7$, 150, and 200 K, respectively, for $\psi = 180°$. The spectral intensity data for each temperature were integrated over the wide energy range from −50 to 125 meV to see the change quantitatively. Figure 5(d) shows the so-obtained intensity profiles. From the image plots and the intensity profiles, we see that at high temperatures the large intensities around M1 and K become weaker while all other regions show slight spectral weight increases. On the other hand, Fig. 5(f) shows the intensity profile of the low-energy region where the integration is from −30 to 30 meV.

Compared with the wide-energy-range intensity profile in Fig. 5(d), the spectral weight increases at high temperatures are more significant. As in the case of Na_2IrO_3, the overall spectral weight moves toward lower energy at high temperatures [18].

In order to see the overall spectral weight distribution over the whole Brillouin zones, the RIXS measurement at
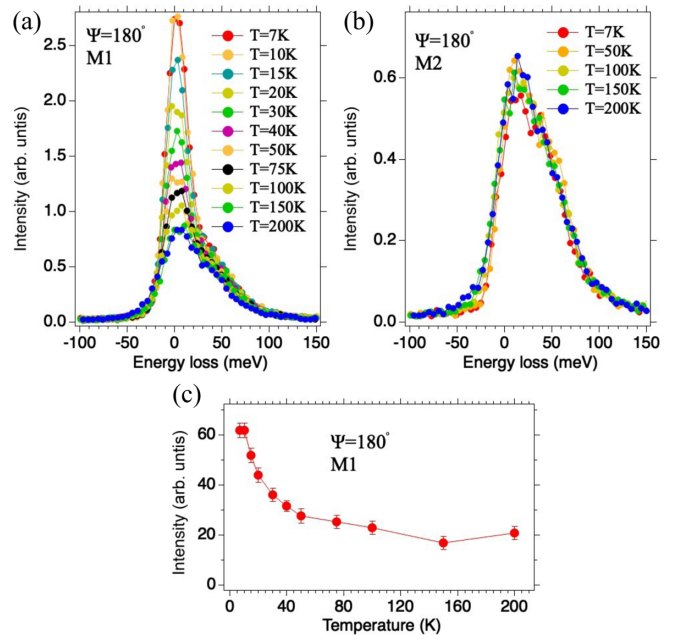

FIG. 4. Temperature dependence of diffuse magnetic Bragg scattering. (a) and (b) RIXS spectra at M1 and M2 ($\psi = 180°$), respectively, taken with varying temperature. (c) Temperature dependence of the elastic scattering intensity of the RIXS spectra at the M1 point.
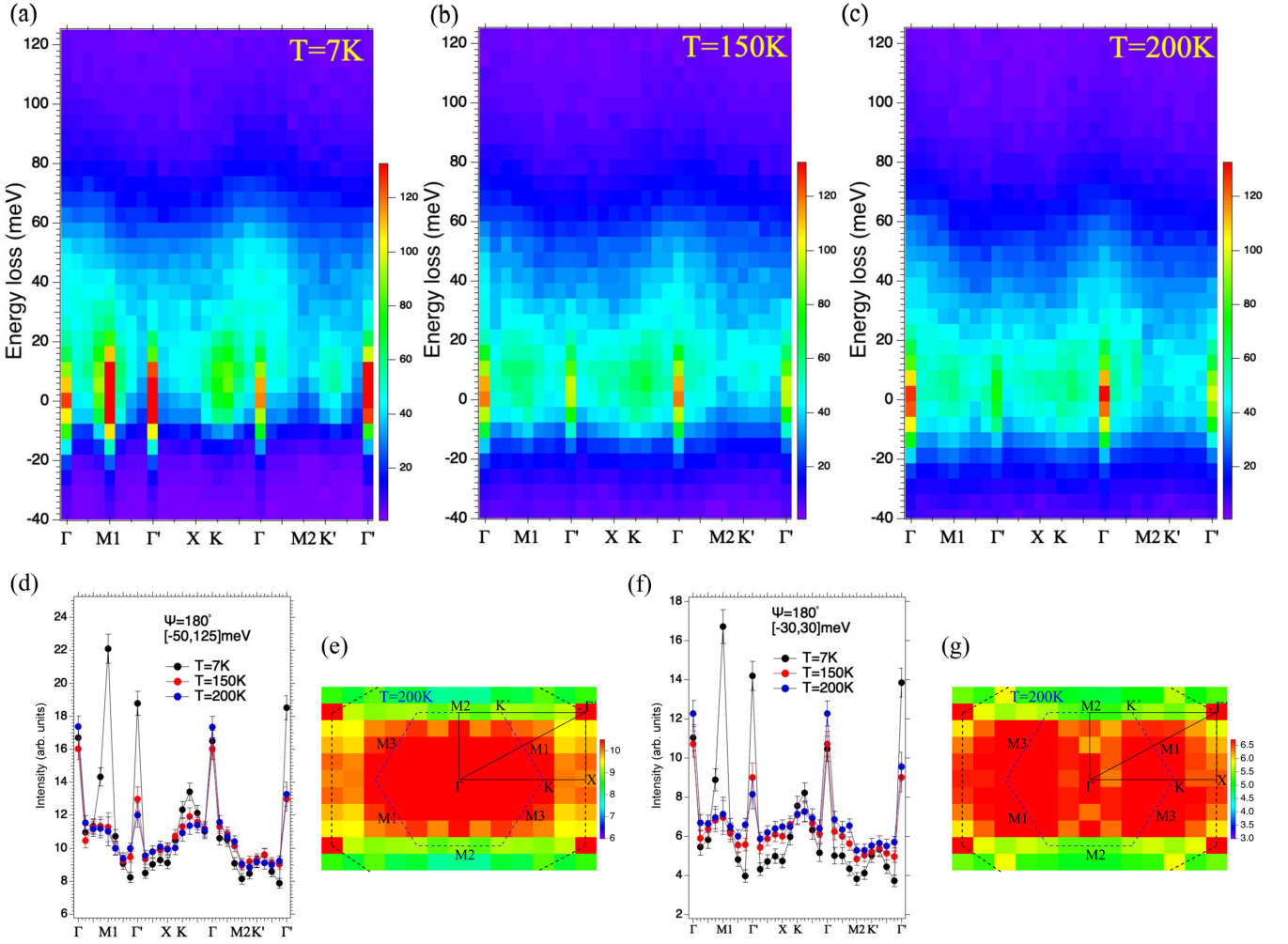
FIG. 5. Temperature evolution of magnetic excitation spectra of $\psi = 180°$. (a) $T = 7$ K, (b) $T = 150$ K, and (c) $T = 200$ K. Spectral intensities in (a)–(c) are integrated over (d) the wide energy region from -50 to 125 meV and (f) the low-energy region from -30 to 30 meV. (e) and (g) Color plots of the integrated intensity of the $T = 200$ K data for $[-50, 125]$ meV and $[-30, 30]$ meV, respectively. The measured data are one quadrant of the solid lines, and the other three quadrants are a reflection of the measured data.

$T = 200$ K was expanded to cover regions other than the high-symmetry lines. Figures 5(e) and 5(g) show the so-obtained color plots of the spectral intensity where the integrated energy ranges are from -50 to 125 meV and from -30 to 30 meV, respectively. The measured data are one quadrant of the solid line region, and the other three quadrants are a reflection of the measured data. Both color plots show that the spectral intensity is not localized at high-symmetry points, but distributed over the broad reciprocal space at high temperature. Higher intensities are seen around Γ within the first Brillouin zone region, while lower intensities are seen in the second Brillouin zone region including the M2-K'-Γ' region except for the large elastic intensity at Γ'. Intermediate intensities are seen in the second Brillouin zone region surrounding the Γ'-X-Γ' region.

IV. DISCUSSION

The Na-deficient Na$_x$IrO$_3$ ($0.6 \leqslant x \leqslant 0.8$) accommodates no long-range magnetic order above 1 K, making its ground state proximate to a possible KQSL [14]. The resonant x-ray scattering measurements in this paper consistently show no

long-range magnetic order above 7 K. However, here we establish that the magnetic excitation spectrum of Na$_x$IrO$_3$ exhibits the same characteristic features as that of Na$_2$IrO$_3$ and thus the same two-dimensional zigzag magnetic correlation exists in Na$_x$IrO$_3$ as in Na$_2$IrO$_3$ in terms of the ordered magnetic moment direction and three dynamically fluctuating zigzag orders [17]. With the aid of theoretical simulations, high-resolution RIXS spectra of Na$_2$IrO$_3$ could be used to confine the parameter regime of the extended Kitaev-Heisenberg model for Na$_2$IrO$_3$ [18]. The parameters of the extended Kitaev-Heisenberg model for Na$_2$IrO$_3$ are in the regime in which the positive off-diagonal exchange Γ is comparable to the strength of the Kitaev exchange $|K|$ and the antiferromagnetic nearest-neighbor Heisenberg exchange is sizable with small long-range interactions of Γ', J_2, and J_3. We suggest that the exchange parameters for Na$_x$IrO$_3$ are in a neighboring regime of those for Na$_2$IrO$_3$.

The outstanding question is what prevents a long-range magnetic order in Na$_x$IrO$_3$. The spin model calculations showed that long-range Heisenberg interactions (J_2 and J_3) play key roles in stabilizing long-range magnetic order in hon-

eycomb Kitaev systems [8,21,22]. The hoppings mediating long-range exchange interactions include indirect exchange paths via the Na ions which can be larger than the direct exchange path [22]. In Na_xIrO_3, the Na sites at the center of the honeycomb ring accommodate all Na vacancies [14]. We suggest that the long-range exchange interactions via Na are weaker in Na_xIrO_3 than in Na_2IrO_3 and a long-range zigzag magnetic order is not realized. The replacement of Na by Li leads to the suppression of the long-range zigzag order [23]. We conjecture that the smaller s orbital extension of the Li ion compared with that of the Na ion contributes to weaker hopping integrals and long-range Heisenberg interactions. In this regard, a partial replacement of Na by Li in Na_xIrO_3 can further weaken the long-range Heisenberg interactions and the zigzag magnetic correlations.

Reference [24] calculated exchange parameters of J, K, Γ, and Γ' as a function of the trigonal splitting which are generic to d^5 Ru and Ir compounds. In these parameter calculations, the larger trigonal splitting in Na_xIrO_3 is expected to give rise to an increase in the strengths of J and Γ' and a decrease in the strength of Γ with a nearly constant K, compared with the case in Na_2IrO_3. Qualitative changes expected due to the structural difference of Na_2IrO_3 and Na_xIrO_3 are consistent with the results of the exchange parameter calculations. The larger Ir-O-Ir angle (99.8°) and Ir-Ir distance (3.1043 Å) in Na_xIrO_3 compared with those (95.9° and 3.072 Å) in Na_2IrO_3 can contribute to a larger J and a smaller Γ, respectively, in Na_xIrO_3 than in Na_xIrO_3 [8,21]. The larger trigonal distortion can lead to an increase in Γ', considering that Γ' is finite due to a trigonal distortion.

Thermodynamic studies of the Kitaev honeycomb materials and models show that the quantum spins can be fractionalized into itinerant Majorana fermions and thermally excited gauge fluxes at intermediate temperature range [25–33]. A RIXS and theoretical study of α-RuCl$_3$ showed the temperature evolution of the equal-time correlation where the Kitaev term dominates the spin correlation at $T = 50$ K and the intensity profile of α-RuCl$_3$ resembles that of the pure Kitaev model [24]. The integrated intensity covering magnetic excitations is a good approximation for the equal-time correlation, $S_{\alpha\alpha} = \langle S_q^\alpha S_{-q}^\alpha \rangle$ ($\alpha = x, y, z$), where q denotes the wave vector [17,24]. In the measurement and sample geometry of $\psi = 180°$, the intensity profile in Fig. 5(e) represents S_{zz} [17,24]. As seen in α-RuCl$_3$, S_{zz} of Na_xIrO_3 at $T = 200$ K resembles S_{zz} of the Kitaev model. This observation indicates that the largest Kitaev interaction in Na_xIrO_3 withstands the thermal fluctuations and reveals the Kitaev physics at high temperature [17,24].

V. CONCLUSION

In this paper, we report orbital and magnetic excitation spectra of Na_xIrO_3 measured using a resonant inelastic x-ray scattering spectrometer. Consistent with the structural refinements, the octahedral and trigonal crystal field splittings are larger in Na_xIrO_3 than in Na_2IrO_3. As found in the physical property measurements, no long-range magnetic order is found above 7 K. However, the diffuse magnetic scattering and azimuth angle dependence of the low-energy spectrum establish that the 2D zigzag magnetic correlations in Na_xIrO_3 are the same as those in Na_2IrO_3 in terms of the ordered magnetic moment direction and three dynamically fluctuating zigzag orders. The Na vacancy at the center of the honeycomb ring is suggested to play a key role in weakening the long-range exchange interactions via the Na ion and preventing the long-range zigzag magnetic order. At high temperature, the intensity map of the equal-time correlation resembles that of the Kitaev model, indicating that Na_xIrO_3 keeps short-range spin correlations of the dominant Kitaev exchange at high temperature.

[1] G. Jackeli and G. Khaliullin, Phys. Rev. Lett. **102**, 017205 (2009).

[2] Y. Singh and P. Gegenwart, Phys. Rev. B **82**, 064412 (2010).

[3] X. Liu, T. Berlijn, W.-G. Yin, W. Ku, A. Tsvelik, Y.-J. Kim, H. Gretarsson, Y. Singh, P. Gegenwart, and J. P. Hill, Phys. Rev. B **83**, 220403(R) (2011).

[4] F. Ye, S. Chi, H. Cao, B. C. Chakoumakos, J. A. Fernandez-Baca, R. Custelcean, T. F. Qi, O. B. Korneta, and G. Cao, Phys. Rev. B **85**, 180403(R) (2012).

[5] S. K. Choi, R. Coldea, A. N. Kolmogorov, T. Lancaster, I. I. Mazin, S. J. Blundell, P. G. Radaelli, Y. Singh, P. Gegenwart, K. R. Choi, S.-W. Cheong, P. J. Baker, C. Stock, and J. Taylor, Phys. Rev. Lett. **108**, 127204 (2012).

[6] J. Chaloupka, G. Jackeli, and G. Khaliullin, Phys. Rev. Lett. **105**, 027204 (2010).

[7] J. G. Rau, E. K.-H. Lee, and H.-Y. Kee, Phys. Rev. Lett. **112**, 077204 (2014).

[8] S. M. Winter, Y. Li, H. O. Jeschke, and R. Valentí, Phys. Rev. B **93**, 214431 (2016).

[9] T. Okubo, K. Shinjo, Y. Yamaji, N. Kawashima, S. Sota, T. Tohyama, and M. Imada, Phys. Rev. B **96**, 054434 (2017).

[10] I. Kimchi and Y.-Z. You, Phys. Rev. B **84**, 180407(R) (2011).

[11] Y. Yamaji, Y. Nomura, M. Kurita, R. Arita, and M. Imada, Phys. Rev. Lett. **113**, 107201 (2014).

[12] K. Shinjo, S. Sota, and T. Tohyama, Phys. Rev. B **91**, 054401 (2015).

[13] E. Sela, H.-C. Jiang, M. H. Gerlach, and S. Trebst, Phys. Rev. B **90**, 035113 (2014).

[14] H. Zhao, B. Hu, F. Ye, M. Lee, P. Schlottmann, and G. Cao, Phys. Rev. B **104**, L041108 (2021).

[15] H. Gretarsson, J. P. Clancy, X. Liu, J. P. Hill, E. Bozin, Y. Singh, S. Manni, P. Gegenwart, J. Kim, A. H. Said, D. Casa, T. Gog, M. H. Upton, H.-S. Kim, J. Yu, V. M. Katukuri, L. Hozoi, J. van den Brink, and Y.-J. Kim, Phys. Rev. Lett. **110**, 076402 (2013).

[16] H. Gretarsson, J. P. Clancy, Y. Singh, P. Gegenwart, J. P. Hill, J. Kim, M. H. Upton, A. H. Said, D. Casa, T. Gog, and Y.-J. Kim, Phys. Rev. B **87**, 220407(R) (2013).

[17] S. H. Chun, J.-W. Kim, J. Kim, H. Zheng, C. Stoumpos, C. Malliakas, J. F. Mitchell, K. Mehlawat, Y. Singh, Y. Choi, T. Gog, A. Al-Zein, M. M. Sala, M. Krisch, J. Chaloupka, G. Jackeli, G. Khaliullin, and B. J. Kim, Nat. Phys. **11**, 462 (2015).

[18] J. Kim, J. Chaloupka, Y. Singh, J. W. Kim, B. J. Kim, D. Casa, A. Said, X. Huang, and T. Gog, Phys. Rev. X **10**, 021034 (2020).

[19] A. Revelli, M. M. Sala, G. Monaco, C. Hickey, P. Becker, F. Freund, A. Jesche, P. Gegenwart, T. Eschmann, F. L. Buessen, S. Trebst, P. H. M. van Loosdrecht, J. van den Brink, and M. Gruninger, Phys. Rev. Research **2**, 043094 (2020).

[20] B. H. Kim, G. Khaliullin, and B. I. Min, Phys. Rev. B **89**, 081109(R) (2014).

[21] S. M. Winter, A. A. Tsirlin, M. Daghofer, J. van den Brink, Y. Singh, P. Gegenwart, and R. Valentí, J. Phys.: Condens. Matter **29**, 493002 (2017).

[22] Y. Sizyuk, C. Price, P. Wölfle, and N. B. Perkins, Phys. Rev. B **90**, 155126 (2014).

[23] G. Cao, T. F. Qi, L. Li, J. Terzic, V. S. Cao, S. J. Yuan, M. Tovar, G. Murthy, and R. K. Kaul, Phys. Rev. B **88**, 220414(R) (2013).

[24] H. Suzuki, H. Liu, J. Bertinshaw, K. Ueda, H. Kim, S. Laha, D. Weber, Z. Yang, L. Wang, H. Takahashi, K. Fürsich, M. Minola, B. V. Lotsch, B. J. Kim, H. Yavaş, M. Daghofer, J. Chaloupka, G. Khaliullin, H. Gretarsson, and B. Keimer, Nat. Commun. **12**, 4512 (2021).

[25] S.-H. Do, S.-Y. Park, J. Yoshitake, J. Nasu, Y. Motome, Y. S. Kwon, D. T. Adroja, D. J. Voneshen, K. Kim, T.-H. Jang, J.-H. Park, K.-Y. Choi, and S. Ji, Nat. Phys. **13**, 1079 (2017).

[26] H. Li, D.-W. Qu, H.-K. Zhang, Y.-Z. Jia, S.-S. Gong, Y. Qi, and W. Li, Phys. Rev. Research **2**, 043015 (2020).

[27] K. Mehlawat, A. Thamizhavel, and Y. Singh, Phys. Rev. B **95**, 144406 (2017).

[28] J. Yoshitake, J. Nasu, and Y. Motome, Phys. Rev. Lett. **117**, 157203 (2016).

[29] J. Yoshitake, J. Nasu, Y. Kato, and Y. Motome, Phys. Rev. B **96**, 024438 (2017).

[30] S. M. Winter, K. Riedl, D. Kaib, R. Coldea, and R. Valentí, Phys. Rev. Lett. **120**, 077203 (2018).

[31] J. Nasu, M. Udagawa, and Y. Motome, Phys. Rev. B **92**, 115122 (2015).

[32] L. J. Sandilands, Y. Tian, K. W. Plumb, Y.-J. Kim, and K. S. Burch, Phys. Rev. Lett. **114**, 147201 (2015).

[33] J. Knolle, D. L. Kovrizhin, J. T. Chalker, and R. Moessner, Phys. Rev. Lett. **112**, 207203 (2014).